



Trace Organic Gas Analyzer Time-of-Flight mass spectrometer (TOGA-TOF) system for airborne observations of formaldehyde

Daun Jeong^{1,a,b}, Rebecca S. Hornbrook^{2,*}, Alan J. Hills², Glenn Diskin³, Hannah S. Halliday³, Joshua P. DiGangi³, Alan Fried⁴, Dirk Richter⁴, James Walega⁴, Petter Weibring⁴, Thomas F. Hanisco⁵, Glenn M. Wolfe⁵, Jason St. Clair⁵, Jeff Peischl^{6,c}, Armin Wisthaler^{7,8}, Tomas Mikoviny⁷, John B. Nowak³, Felix Piel⁷, Laura Tomsche³, Christopher D. Holmes⁹, Amber Soja³, Emily Gargulinski¹⁰, James H. Crawford³, Jack Dibb¹¹, Carsten Warneke¹², Joshua Schwarz¹², and Eric C. Apel^{2,*}

¹Advanced Study Program, NSF National Center for Atmospheric Research, Boulder, CO, USA

²Atmospheric Chemistry Observations & Modeling Laboratory, NSF National Center for Atmospheric Research, Boulder, CO, USA

³NASA Langley Research Center, Hampton, VA, USA

⁴Institute of Arctic and Alpine Research, University of Colorado, Boulder, CO, USA

⁵NASA Goddard Space Flight Center, Greenbelt, MD, USA

⁶Cooperative Institute for Research in Environmental Sciences, University of Colorado, Boulder, CO, USA

⁷Department of Chemistry, University of Oslo, Oslo, Norway

⁸Institute for Ion Physics and Applied Physics, University of Innsbruck, Innsbruck, Austria

⁹Department of Earth, Ocean, and Atmospheric Science, Florida State University, Tallahassee, FL, USA

¹⁰National Institute of Aerospace, Hampton, VA, USA

¹¹Earth Systems Research Center, University of New Hampshire, Durham, NH, USA

¹²Chemical Science Laboratory, National Oceanic and Atmospheric Administration (NOAA), Boulder, CO, USA

^anow at: Cooperative Institute for Research in Environmental Sciences, University of Colorado, Boulder, CO, USA

^bnow at: Chemical Science Laboratory, National Oceanic and Atmospheric Administration (NOAA), Boulder, CO, USA

^cnow at: Global Monitoring Laboratory, National Oceanic and Atmospheric Administration (NOAA), Boulder, CO, USA

*Corresponding Authors: Eric C. Apel and Rebecca S. Hornbrook
Atmospheric Chemistry Observations & Modeling Laboratory,
NSF National Center for Atmospheric Research, Boulder, CO 80307 USA
apel@ucar.edu
rsh@ucar.edu

Keywords: FIREX-AQ, formaldehyde, TOGA-TOF, biomass burning



41 **Abstract**

42 Formaldehyde (HCHO) is a ubiquitous atmospheric constituent, originating from primary
43 emissions (natural and anthropogenic) and secondary production via the oxidation of volatile
44 organic compounds (VOCs). In addition to being a regulated pollutant, HCHO is a key species
45 used as a tracer of recent photochemical activity due to its short atmospheric lifetime and its role
46 as a source of HO_x radicals. Given its diverse sources and high spatial variability, HCHO is
47 challenging to represent accurately in chemical transport models, often resulting in significant
48 discrepancies with observations. Airborne in-situ measurements of HCHO, especially when
49 combined with VOC precursor data, offer valuable insights into its atmospheric distributions for
50 evaluating models. Here, we present HCHO observations from the NSF NCAR Trace Organic
51 Gas Analyzer with Time-of-Flight mass spectrometer (TOGA-TOF), deployed during the 2019
52 Fire Influence on Regional to Global Environments and Air Quality (FIREX-AQ) campaign.
53 While most HCHO instruments target at most a few selected species for measurement, the TOGA-
54 TOF employs a rapid gas chromatography-mass spectrometry (GC/MS) technique and provides
55 discrete VOC measurements—including >100 C₁–C₁₀ species—at a time resolution of less than
56 2 minutes. We compare TOGA-TOF HCHO data to measurements from three 1-Hz instruments
57 aboard the NASA DC-8: the Compact Atmospheric Multi-species Spectrometer (CAMS), the In
58 Situ Airborne Formaldehyde (ISAF) instrument, and a proton-transfer-reaction time-of-flight
59 mass spectrometer (PTR-ToF-MS). The wide dynamic range of observed HCHO concentrations
60 (from < 100 ppt to ~100 ppb) during FIREX-AQ enabled a robust intercomparison. TOGA-TOF
61 HCHO agreed well with CAMS (slope = 1.1), with similar agreement with the PTR-ToF-MS,
62 while larger discrepancies were observed with ISAF (slope = 1.5), likely due to differences in
63 calibrations. Normalized excess mixing ratios (NEMRs) of HCHO relative to CO in wildfire
64 plumes exhibited consistent trends with plume age across instruments. These findings highlight
65 the TOGA-TOF's capability for highly sensitive and accurate airborne HCHO measurements.

66 **1. Introduction**

67 Formaldehyde (HCHO) is one of the most ubiquitous non-methane volatile organic
68 compounds (VOCs) in the atmosphere. In addition to being an EPA regulated pollutant (National
69 Research Council (US) Committee on Toxicology, 1980), HCHO is a key reactive compound in



70 understanding recent photochemistry in the atmosphere. HCHO is an oxidation product of a wide
71 range of VOCs, has a relatively short lifetime, and is an important source of HO_x (OH + HO₂),
72 therefore affecting NO_x-VOC-O₃ chemistry (Seinfeld and Pandis, 2006). Globally, the dominant
73 source of HCHO is secondary production from VOC oxidation (Luecken et al., 2012; Stavrakou
74 et al., 2009). Tropospheric background levels of HCHO are maintained through methane (CH₄)
75 (Stavrakou et al., 2009) and isoprene (C₅H₈) (Curci et al., 2010; Luecken et al., 2018; Palmer et
76 al., 2003; Wolfe et al., 2016) oxidation. Direct emissions of HCHO can also be important locally;
77 sources include vehicle emissions (Possanzini et al., 2002; Sagebiel et al., 1996; Viskari et al.,
78 2000), biomass burning (Lee et al., 1997; Zhang et al., 2013), and fossil fuel industries (Fried et
79 al., 2020; Green et al., 2021; Pfister et al., 2019). In the atmosphere, HCHO is mainly lost through
80 photolysis, reaction with OH, and deposition, resulting in daytime atmospheric lifetimes of 1 to 9
81 hours (1–3 hours midday).

82 As an important proxy for understanding recent photochemistry, HCHO observations have
83 been used to indicate ozone sensitivity regimes (VOC- or NO_x-limited) (Duncan et al., 2010;
84 Martin et al., 2004; Nussbaumer et al., 2021; Schroeder et al., 2017; Souri et al., 2020, 2023) as
85 well as top-down estimations of isoprene (Cao et al., 2018; Kaiser et al., 2018; Palmer et al., 2003;
86 Wolfe et al., 2016; Zhu et al., 2016) and anthropogenic VOC (Cao et al., 2018; Kwon et al., 2021)
87 emissions. While satellite retrievals of HCHO column densities have been widely used in these
88 methods, challenges remain in capturing the spatial (vertical and horizontal) representation of
89 HCHO over the wide mixing ratio (MR) range observed in the troposphere; HCHO MRs can vary
90 less from than 20 parts per trillion (ppt) in remote regions, 1–20 parts per billion (ppb) in urban
91 environments, and > 100 ppb in fire plumes as observed from aircraft. These challenges in HCHO
92 satellite observations have been driven by uncertainties in retrieval methods (Anderson et al., 2017;



93 Liao et al., 2025; Sourì et al., 2023; Stavrakou et al., 2009; Zhu et al., 2016), instrument sensitivity
94 (Sourì et al., 2023), and coarse pixel sizes (Kwon et al., 2021; Sourì et al., 2023). Uncertainties in
95 satellite observations increase in environments with low HCHO, such as regions with weak
96 biogenic or anthropogenic sources (Sourì et al., 2023). Three-dimensional chemical transport
97 models may also fail to reproduce observed HCHO levels due to inaccurate emission inventories
98 of direct HCHO emissions or its VOC precursors (Green et al., 2021; Jaeglé et al., 2018; Luecken
99 et al., 2012, 2018; Warneke et al., 2007), uncertainties in chemical mechanisms (Luecken et al.,
100 2012), and coarse grid size. High quality *in-situ* HCHO observations during airborne field
101 campaigns can provide useful information to validate satellite observations and evaluate chemical
102 transport models (Anderson et al., 2017; Chan Miller et al., 2017; Schroeder et al., 2017; Sourì et
103 al., 2023; Zhu et al., 2016). For example, recent studies on HCHO intercomparisons between
104 satellite and *in-situ* airborne observations showed that satellite HCHO retrievals can have a
105 systematic low bias of -20 to -51% (Anderson et al., 2017; Zhu et al., 2016), which can lead to
106 underestimation of VOC emissions. These systematic biases in satellite observations can be
107 corrected using high-quality airborne *in-situ* observations of HCHO (Chan Miller et al., 2017; Zhu
108 et al., 2016, 2017).

109 Biomass burning produces large amounts of HCHO both from primary emissions and
110 secondary production. During a biomass burning event, a highly complex mixture of VOCs (Akagi
111 et al., 2011; Gilman et al., 2015; Gkatzelis et al., 2024; Koss et al., 2018; Travis et al., 2023;
112 Yokelson et al., 2013a) is produced from the fire source, which subsequently undergoes complex
113 chemical (i.e., reaction with oxidants and photolysis) and physical (i.e., dilution and cooling)
114 transformations downwind of the source (Decker et al., 2021; Hornbrook et al., 2011; Robinson et
115 al., 2021; Wang et al., 2021). For the recent joint NOAA/NASA Fire Influence on Regional to



116 Global Environments and Air Quality (FIREX-AQ) mission, Wang et al. (2021) used a high-
117 resolution large eddy simulation (LES) to show the chemical complexity of a fresh wildfire plume.
118 The levels and types of predominant oxidants, which are dependent on the historic exposure to
119 light, varies with the evolution of a plume, affecting the chemistry and fate of trace gases and
120 aerosols (Decker et al., 2021; Robinson et al., 2021; Wang et al., 2021). Liao et al. (2021) showed
121 that primary emissions of HCHO dominate near the fire source but secondary production from
122 VOC oxidation becomes important (up to ~ 60% after a few hours of physical age) as the fire ages.
123 As reported by Travis et al. (2023), the MRs of different types of VOCs emitted in crop and
124 prescribed fire plumes during FIREX-AQ depends on fuel types and fire states. The physical and
125 chemical complexities in fire plumes ensure that HCHO MRs are highly dynamic presenting
126 challenges for satellite retrievals (Stavrakou et al., 2009) and models to accurately represent local
127 and regional distributions of HCHO.

128 In this study, we present the NSF NCAR Trace Organic Gas Analyzer Time-of-Flight mass
129 spectrometer (TOGA-TOF) as a fast online GC/MS (gas chromatography-mass spectrometry)
130 technique for airborne observations of HCHO. Studies on improved techniques to detect HCHO
131 have been ongoing, attesting to its analytical challenges (Gilpin et al., 1997; Hopkins et al., 2003;
132 Hunter et al., 1999; Rice and Quay, 2006). While most currently available instrumental techniques
133 are specialized in detecting HCHO, the TOGA-TOF routinely measures over a hundred VOCs
134 using a non-reactive concentration technique, with the capability to analyze untargeted
135 compounds. Thus, TOGA-TOF is a unique airborne standalone instrument for the identification
136 and quantification of a wide range of C₁–C₁₀ VOCs, including formaldehyde, in complex ambient
137 air samples. The NOAA/NASA FIREX-AQ campaign (July to September 2019) was the first
138 campaign in which the TOGA-TOF was deployed for airborne measurements. During FIREX-AQ,



we had the opportunity to measure alongside two state-of-the-art HCHO measurement systems aboard the NASA DC-8 during the entire FIREX-AQ campaign: the NASA In Situ Airborne Formaldehyde (ISAF) instrument (Cazorla et al., 2015) and the University of Colorado Compact Atmospheric Multi-species Spectrometer (CAMS) (Richter et al., 2015). The University of Oslo Proton-Transfer Reaction Time-of-Flight Mass Spectrometer (UiO PTR-ToF-MS) (Müller et al., 2014) measured HCHO for select time periods as well. For this study, we present the TOGA-TOF HCHO data and focus on intercomparisons with CAMS and ISAF but also include comparisons with the UiO PTR-ToF-MS. The FIREX-AQ dataset is an excellent testbed to compare a wide range of HCHO mixing ratios (below 100 ppt to ~100 ppb) in a spatially variable ambient atmosphere. The technique used in the TOGA-TOF could, in principle, be implemented in many existing online GC/MS systems for semi-routine measurements of HCHO.

2. Methods

The sample preconcentration system in the TOGA-TOF is similar to the earlier generation TOGA instrument with a quadrupole mass analyzer, which has been described in the literature (Apel et al., 2015). The TOGA-TOF has been extensively characterized in the lab prior to and post FIREX-AQ. Here, we describe the basic operation techniques of the TOGA-TOF system (Sect. 2.1), summarize the HCHO measurements during FIREX-AQ (Sect. 2.2), calculate the weighted averages for direct comparisons between instruments with different sampling time resolution (Sect. 2.3), and derive normalized excess mixing ratios (NEMR) of HCHO from selected plume transects (Sect. 2.4).



159 **2.1 Description of the NSF NCAR Trace Organic Gas Analyzer with Time-of-Flight Mass** 160 **Spectrometer (TOGA-TOF)**

161 The TOGA-TOF hardware consists of a cryogenic preconcentration system, gas
162 chromatograph (GC), time-of-flight (TOF) mass analyzer (TOFWERK, Switzerland), electronics
163 box, clean air generator and on-board calibration system (CAG), and pump box. All major
164 components except the TOF mass analyzer are custom built. Typical preconcentration and GC
165 analysis sequences for the system are shown in **Fig. 1** and the flows for each sequence are shown
166 in **Fig. 2**. The GC analysis, including temperature ramp and cool and sample preconcentration
167 steps, occur simultaneously, with the full cycle duration of both processes time synced (**Fig. 1**) to
168 less than 2 min. During FIREX-AQ, the runtime for one full cycle was 105 seconds including 33
169 seconds of sample collection (i.e., “sampling”). The preconcentration system consists of three
170 cryogenically-cooled traps as described by Apel et al. (2015): (1) a water trap for removal of water
171 in ambient sampled air, (2) a sample trap for enrichment of targeted VOCs in ambient air, and (3)
172 a cryofocusing trap to refocus the analytes prior to injection into the GC. Corresponding to each
173 temperature setpoint described in **Fig. 1**, the cooling of each trap is achieved by metering the flow
174 of gas-phase N₂ generated from the headspace of the TOGA-TOF Dewar through coils at the
175 bottom of the dewar that were immersed in liquid N₂ (Apel et al., 2015). To heat the traps, the cold
176 N₂ gas flow was first shut off and followed by PID controlled flow of electricity, via a
177 WATLOW™ (Anafaze MLS300) temperature controller, through resistive wires wrapped around
178 the traps. The sample trap is packed with glass wool to allow greater surface area for the
179 enrichment of VOCs when cooling the trap to -140°C (**Fig. 1**), while allowing bulk gases such as
180 oxygen and nitrogen to pass through unretained. Both the water trap (inner diameter (I.D.) = 0.04
181 in.) and cryofocusing trap (I.D. = 0.021 in.) are open tubes.

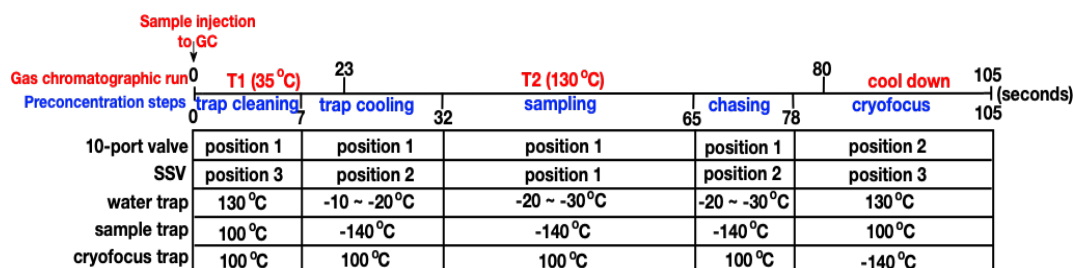


Figure 1. TOGA-TOF operational sequences for the gas chromatograph temperature program (red) and the preconcentration steps (blue). The position of the valves (10-port valve and stream selector valve; SSV) and temperatures of each trap are shown for each step. The duration of each sequence corresponds to the normal sampling mode timing during FIREX-AQ.

182

183 For chromatography, a Restek MXT-624 column (I.D. = 0.18 mm, length = 8 m) is used
 184 with helium as the carrier gas. The GC column has two temperature set points with temperatures
 185 ranging between 35°C and 130°C (**Fig. 1**), also controlled by the Watlow, allowing gas-phase C₁
 186 to C₁₀ VOCs to sequentially elute from the column. This allows the separation of VOCs, including
 187 many structural isomers with the same chemical formula, based on their differences in interaction
 188 with the stationary phase of the column. For detection of VOCs, the GC is coupled to a high-
 189 resolution electron ionization time-of-flight mass spectrometer (HR EI-TOF-MS; TOFWERK),
 190 using 70 eV ionization resulting in classical electron ionization (EI) spectra of the compounds.
 191 This methodology allows routine quantification of well over 100 VOCs with the ability to further
 192 analyze additional C₁ to C₁₀ compounds within the detectable range. Fluctuations in sensitivity are
 193 corrected by normalizing with ambient levels of tetrachloromethane (CCl₄). Background
 194 corrections are made by system generated ultra-pure helium (“He mode”) and zero-air blanks and
 195 then subtracting average blank peak areas from ambient samples. For all surfaces that the sample
 196 contacts, Restek Sulfinert® steel tubing is used to minimize interactions. Data processing is
 197 performed using Tofware (Aerodyne Research, Inc., Billerica, MA) for high resolution peak fitting



198 and TERN-in-IGOR (Claflin et al., 2021; Isaacman-VanWertz et al., 2017; Lerner et al., 2017)
199 (Aerodyne Research, Inc.) for chromatographic peak analysis.

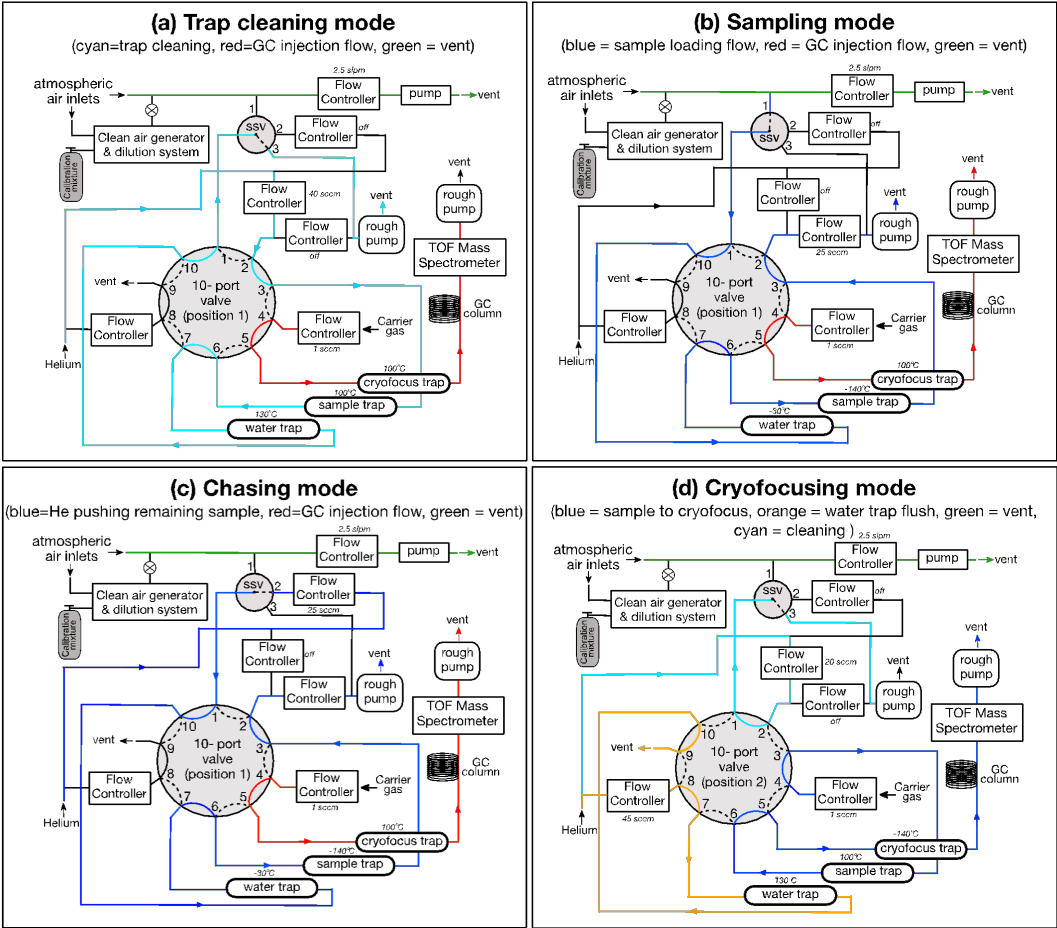


Figure 2. Simplified flow diagram of TOGA-TOF showing flows and temperatures of each trap during (a) trap cleaning mode, (b) sampling mode, (c) chasing mode, and (d) cryofocusing mode, corresponding to the sequence in Fig. 1.

2.2 Description of HCHO and CO measurements during FIREX-AQ

In this section, we describe the TOGA-TOF HCHO measurements during FIREX-AQ (July–September 2019). FIREX-AQ (Warneke et al., 2023; https://asdc.larc.nasa.gov/project/FIREX-AQ) focused on the emissions of trace gases and



205 particles from wildland, prescribed, and agricultural fires in the United States. The NASA DC-8
 206 flights during FIREX-AQ were based out of Boise, ID, mainly focusing on Western U.S. fires, and
 207 Salina, KS, focusing on southeastern U.S. agricultural fires (flight tracks shown in **Fig. S1**). Details
 208 on the field campaign may be found in Warneke et al. (2023).

209 As described in **Sect. 2.1**, the TOGA-TOF uses electron ionization for the detection of
 210 VOCs. The EI of HCHO results in a spectrum of its parent ion (m/z 30) and major fragments (m/z
 211 28 and 29) (**Fig. S2a**). **Figure S2b** shows the chromatographic signals of CH_2O^+ (m/z 30; exact
 212 mass 30.010016 amu) and CHO^+ (m/z 29; exact mass 29.002191 amu) eluting at ~ 20 s. The high
 213 resolution (HR)-TOF allows detection of highly resolved ions and the Tofware peak fitting
 214 analysis shows separate parent and dominant fragments from other adjacent peaks (**Fig. S2c**).
 215 HCHO calibration was carried out using a HCHO in N_2 gas-phase mixture contained in a treated
 216 aluminum cylinder (Apel-Riemer Environmental, Inc.), diluted with ultra-high purity N_2 . The
 217 stated HCHO concentration of the calibration mixture cylinder from the company was 1.69 ppmv.
 218 The concentration was checked using three independent methods within a two-month period using:
 219 (1) Fourier transform infrared spectroscopy (FTIR – NSF NCAR ACOM direct absorption using
 220 the Beer-Lambert law, 1.55 ppmv), (2) Mid-IR – University of Colorado - also direct absorption
 221 employing the CAMS instrument (1.65 ppm), and (3) an EPA 2,4-dinitrophenylhydrazine (DNPH)
 222 cartridge method (1.64 ppmv). For methods (1) and (2), quantification of HCHO relies on the
 223 absolute IR cross section and thus does not require an external standard. Therefore, these can be
 224 regarded as fully independent reference methods. For the calibration of TOGA-TOF we used the
 225 averaged value of 1.61 ppmv from the three quantification methods, and the resulting calibration
 226 curve is shown in **Fig. S3**. The TOGA-TOF HCHO lower limit of detection (LLOD) during
 227 FIREX-AQ was 20 ppt, and the HCHO measurement had an uncertainty of 35% based on the



228 variability of repeat calibrations using a 1.6 ppm (parts per million) HCHO in N₂ standard mixture
229 and a 90 ppb HCHO in N₂ standard mixture (both Apel-Reimer, Inc.), dynamically diluted to MRs
230 ranging between 0.15 and 100 ppb using (1) the CAG (i.e., catalytically-scrubbed ambient air), (2)
231 dry N₂, and (3) humidified N₂. No humidity dependence was observed.

232 HCHO mixing ratios from the TOGA-TOF were compared to 1-Hz HCHO measurements
233 from the ISAF, CAMS, and UiO PTR-ToF-MS instruments onboard the DC-8. The ISAF
234 instrument was operated by NASA and the details on the instrumental technique are described in
235 Cazorla et al. (2015). Briefly, the ISAF instrument uses a laser-induced fluorescence technique to
236 quantify HCHO using the fluorescence resulting from excitation of HCHO at 353 nm with a
237 tunable UV laser. Backgrounds were determined from the offline position 0.005 nm away from
238 the peak. Calibrations were made using a compressed HCHO gas cylinder (Air Liquide, 584 ppbv)
239 quantified by FTIR (Liao et al., 2021). ISAF was operated at a native sampling rate of 10 Hz and
240 archived at 10 Hz and 1 Hz. We used the 1-Hz data for analysis. The reported LLOD of HCHO
241 measured by ISAF is 30 ppt for the 1-Hz data at a signal/noise = 1 and the accuracy (systematic
242 uncertainty) of the ISAF measurements is estimated to be 10% + 10 ppt. More details on the ISAF
243 HCHO measurement during FIREX-AQ can be found in Liao et al. (2021).

244 The CAMS was operated by the University of Colorado and a detailed description of the
245 system can be found in the work of Richter et al. (2015). The CAMS uses a tunable IR laser source
246 for generation of mid-IR light for the detection of HCHO based on absorption. Background spectra
247 were collected during flights using zero air from a scrubber and were subtracted from the ambient
248 spectra. Calibrations were carried out by using a 4.9 ppm HCHO standard in N₂, quantified by
249 direct absorption using the Beer-Lambert law. The reported uncertainty of the FIREX-AQ HCHO
250 CAMS measurements is 6% and the campaign averaged LLOD is 110 ppt for 1-Hz measurements



251 at a signal/noise = 1 during FIREX-AQ. However, during previous airborne missions (e.g.,
252 KORUS-AQ; Fried et al., 2020), LLODs ranging from 28 to 80 ppt have been reported. The
253 degraded performance during FIREX-AQ resulted from dirty multipass cell mirrors.

254 The UiO PTR-ToF-MS (Müller et al., 2014) was operated by the University of Oslo with
255 a focus on measuring NH_3 during FIREX-AQ, although HCHO and a number of additional VOCs
256 were reported for select flights (i.e., 25 July and 3 August). The PTR-ToF-MS uses hydronium
257 ions (H_3O^+) generated from water vapor in a glow discharge-drift-tube to detect VOCs through
258 nondissociative proton transfer reactions. HCHO calibrations were carried out using a gas-phase
259 HCHO in N_2 cylinder (Apel-Riemer Environmental, Inc., 9.6 ppm HCHO; $\pm 5\%$). This calibration
260 was checked post-mission by generating test atmospheres with five different HCHO mixing ratios
261 (145–1035 ppb) in a 250-L laboratory chamber. The chamber was equipped with a White cell type
262 multiple reflection mirror system with a 120-m optical path length for online detection with a
263 Bruker IFS 66v/S FTIR instrument. The two methods were in excellent agreement, with the PTR-
264 ToF-MS reporting a volume mixing ratios less than 3% higher than the FTIR. During the two flight
265 days (25 July and 3 August) the UiO PTR-ToF-MS measured HCHO; the slope of the retrieved
266 ambient HCHO relative to that from CAMS was 1.03.

267 Normalized excess mixing ratios (NEMRs) of HCHO to CO are calculated as described in
268 **Sect. 2.4**. CO measurements were made onboard the DC-8 using the NOAA Los Gatos Research
269 (LGR) CO instrument and the NASA Differential Absorption Carbon monOxide Measurement
270 (DACOM) instruments. The LGR instrument (Bourgeois et al., 2022) uses an infrared laser off-
271 axis integrated-cavity-output spectroscopy technique with a time response of 1 Hz. The DACOM
272 instrument uses a differential absorption technique with an infrared tunable diode laser detecting
273 CO at the 4.7 μm wavelength, giving a data frequency of 5 Hz and measurement uncertainty of



274 2% (Sachse et al., 1987). The two CO instruments were in excellent agreement with the coefficient
 275 of determination $r^2 = 0.97$, and a slope of 0.97 during the entirety of the campaign (**Fig. S4**), with
 276 the reported LGR CO consistently 2.2% below that of DACOM.

277 **2.3 Averaging methods for comparison of HCHO between different instruments**

278 Data averaging across various sampling time periods is often carried out for direct
 279 comparison between instrumental techniques with different sample integration times. **Figure 3**
 280 shows HCHO measured by TOGA-TOF and ISAF with LGR CO measurements during plume
 281 transects from the Castle Fire (**Fig. 3a**) and the Williams Flats Fire (**Fig. 3b**). As described in **Sect.**
 282 **2.1**, during FIREX-AQ, the TOGA-TOF took discrete samples for 33 seconds in a 105-second
 283 cycle period; therefore, subsections of each plume transect were sampled for analysis (**Fig. 3**). To
 284 directly compare the discrete TOGA-TOF HCHO sampling data, CAMS, ISAF, and UiO PTR-
 285 ToF-MS 1-Hz HCHO data are averaged over the time during which the TOGA-TOF sampling
 286 occurred. Here we use two averaging methods for HCHO comparison: (1) normal averaging and
 287 (2) volume-weighted averaging. The normal averaging is performed by taking the arithmetic mean
 288 of the 1-Hz source data measured between the start and stop times of TOGA-TOF sampling. Below
 289 LLOD values of the source data are included in the averaging. A minimum of at least one valid
 290 (i.e., measured value or below LLOD) 1-Hz source data point during the TOGA-TOF sampling
 291 period is allowed for the analysis to produce a non-missing merged value. This algorithm is how
 292 the NASA online merging tool generates the TOGA.DC8_MRG and is publicly available on the
 293 NASA Langley Research Center (LaRC) Airborne Science Data repository at [https://www-](https://www-air.larc.nasa.gov/cgi-bin/ArcView/firexaq?MERGE=1#TOGA.DC8_MRG/)
 294 [air.larc.nasa.gov/cgi-bin/ArcView/firexaq?MERGE=1#TOGA.DC8_MRG/](https://www-air.larc.nasa.gov/cgi-bin/ArcView/firexaq?MERGE=1#TOGA.DC8_MRG/). More details on the
 295 NASA online merging tool can be found in [https://www-](https://www-air.larc.nasa.gov/missions/etc/onlinemergedoc.pdf)
 296 [air.larc.nasa.gov/missions/etc/onlinemergedoc.pdf](https://www-air.larc.nasa.gov/missions/etc/onlinemergedoc.pdf).

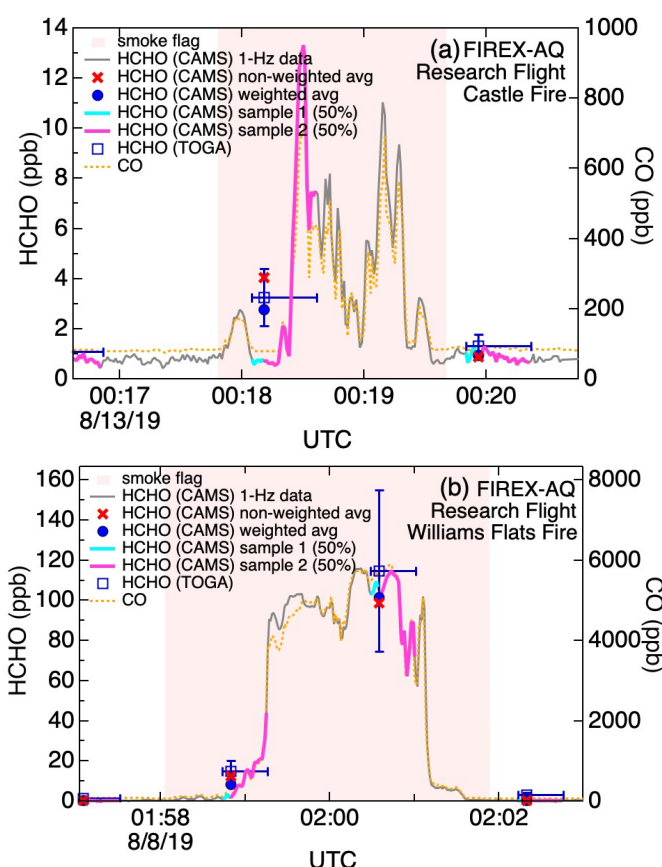


Figure 3. Example time series of ISAF and TOGA-TOF HCHO and LGR CO observations during FIREX-AQ transverse (i.e., perpendicular to the transport of the fire plume) plume transects with relatively (a) high and (b) low variability in the observed 1-Hz HCHO. The pink shading shows when the DC-8 was inside the smoke plume based on the relative changes in CO. Vertical error bars on the TOGA-TOF HCHO data points show the measurement uncertainty ($\pm 35\%$), centered on the TOGA-TOF sampling time midpoint, and the horizontal error bars span the start to stop times of each TOGA-TOF sample. For each of the start-to-midpoint and midpoint-to-stop times of the TOGA-TOF sampling periods, 50% of the total sample volume occurred. These times (start/midpoint/stop) were used for deriving weighted averages of the 1-Hz HCHO and CO data.

The second averaging method is the volume-weighted averaging method based on the volume of air sampled. During TOGA-TOF sampling, the flow rate through the sample trap was variable, with faster relative flow rates at the beginning of each sample. We define a midpoint, as shown in **Fig. 3**, at which the sample volume reached 50% of the total volume during the corresponding sampling cycle. The midpoint is calculated for each sample by determining the total



sample volume collected for samples with varying sampling durations, and then the relationship between the total sampling time and the sample volume to determine the time at which half the sample volume was collected. The midpoints determined through this method are reported in the TOGA-TOF FIREX-AQ data files archived at the NASA Atmospheric Science Data Center (ASDC) (https://doi.org/10.5067/ASDC/FIREXAQ_TraceGas_AircraftInSitu_DC8_Data_1). The arithmetic mean of the 1-Hz data is thus calculated for the time periods between the start to midpoint (T_1) and midpoint to stop times (T_2), and these two means are averaged to weight the merge value on the sampled volume.

When sampling near strong VOC sources (e.g., wildfires or urban emissions), air masses often have significant heterogeneity of HCHO levels from varying direct emissions and photochemical production from rapidly changing VOC precursors. In those cases, using the non-weighted averages of 1-Hz measurements can lead to significant biases when they are directly compared to the TOGA-TOF data. Therefore, using volume-weighted averages of higher-frequency data that factor in the true sample volume midpoints for comparisons with TOGA-TOF data allows a more accurate comparison of the sampled air masses.

Using the above methodology, volume-weighted averages of LGR and DACOM 1-Hz CO data are carried out, during the times when TOGA was sampling. In our study, we use the volume-weighted averaged LGR CO data when it is available, and for times when it is not available, we use the volume-weighted averaged DACOM CO data multiplied by 0.978 to account for the relative differences in the two CO datasets. We normalized to the LGR CO data as it is a little lower to be conservative in our analyses, although the two CO datasets are in excellent agreement (**Fig. S4**) and within the combined measurement uncertainties (2 ppb + 2% for LGR, and typically $\pm 2\%$ for DACOM.)



339 2.4 Formaldehyde Normalized Excess Mixing Ratios

340 We compare HCHO normalized excess mixing ratios (NEMRs) for Western U.S. wildland
 341 fires calculated using HCHO reported by TOGA-TOF, ISAF, and CAMS. There are several ways
 342 to derive NEMRs (Yokelson et al., 2013a) and here we used the slope method, which involves
 343 determining the slope of HCHO in ppt against CO in ppb for a single plume transect and the
 344 background air outside the plume. CO was used as the reference species to normalize for dilution
 345 as it is a conserved biomass burning tracer in wildfire plumes (Müller et al., 2016; Selimovic et
 346 al., 2019; Yokelson et al., 2013a). For the NEMRs from CAMS and ISAF, we use the 1-Hz HCHO
 347 and CO data for the entire plume transect. For the TOGA-TOF NEMRs, we use the discrete HCHO
 348 sampling points, which range between two and ten samples for each plume transect--including a
 349 background sample and plotted these against the volume-weighted average (described in **Sect. 2.4**)
 350 TOGA merged CO for corresponding sampling periods.

351 The NEMR analysis was carried out for the plumes selected based on the following criteria:
 352 a) plume transects perpendicular to the fire source, b) availability of at least one full TOGA-TOF
 353 sampling cycle within the plume, c) stable background HCHO prior to and after the plume transect,
 354 and d) availability of both CAMS and ISAF 1-Hz HCHO data sets and CO for both background
 355 and in-plume sampling. Fire plumes were identified via plume flags using above background CO
 356 in addition to visual inspection of the data (FIRE_FLAG_TABULAR_DATA.dat, [https://www-](https://www-air.larc.nasa.gov/cgi-bin/ArcView/firexaq#SCHWARZ.JOSHUA/)
 357 [air.larc.nasa.gov/cgi-bin/ArcView/firexaq#SCHWARZ.JOSHUA/](https://www-air.larc.nasa.gov/cgi-bin/ArcView/firexaq#SCHWARZ.JOSHUA/)). Based on these criteria,
 358 NEMRs were calculated for a total of 86 plume transects from 7 fire sources in the Western U.S.
 359 and these are summarized in the supporting information (**Table S1**).

360 3. Results and Discussion

361 3.1 Comparison of HCHO between different instrumental techniques



362 Direct intercomparisons of measured HCHO between TOGA-TOF and the 1-Hz
 363 instruments were carried out for data collected during all flights with available HCHO observations
 364 onboard the DC-8. This included 13 flights sampling Western U.S. fires, 7 flights in the
 365 Southeastern U.S., and 2 transit flights (**Fig. S1**). The dataset allowed comparisons of the widest
 366 possible range of HCHO observed in the troposphere (below 100 ppt to ~ 100 ppb). **Figure 4**
 367 shows correlations between TOGA-TOF, CAMS, and ISAF HCHO, averaged during the
 368 corresponding TOGA-TOF sampling periods. Comparisons with normal averaged 1-Hz HCHO
 369 (**Fig. 4a** and **b**) and volume-weighted averaged 1-Hz HCHO (**Fig. 4c** and **b**), described in **Sect.**
 370 **2.3**, are both shown. The data points are colored according to the relative standard deviation of
 371 HCHO, calculated as the standard deviation of 1-Hz HCHO data during the TOGA-TOF sampling
 372 period divided by the HCHO measured by TOGA-TOF. This relative standard deviation represents
 373 the variability of the 1-Hz HCHO data during the TOGA-TOF sampling period.

374 Both non-weighted (**Fig. 4a**) and volume-weighted (**Fig. 4c**) averages showed that HCHO
 375 measured by CAMS was within the 35% measurement uncertainty of the TOGA-TOF while the
 376 comparisons with ISAF (**Fig. 4b** and **d**) were outside of the range of measurement uncertainties.
 377 When using the non-weighted averaging method (**Fig. 4a** and **b**), the bivariate fitting (orthogonal
 378 distance regression, ODR) of the TOGA-TOF and the 1-Hz HCHO gave a slope of 1.2 for CAMS
 379 (y -intercept -177.4 ppt, **Fig. 4a**) and 1.6 for ISAF (y -intercept -210.2 ppt, **Fig. 4b**). The y -axis
 380 residuals from the ODR fit were largest for data points with higher relative standard deviations
 381 (i.e., > 0.7) of HCHO. For the non-weighted averages, the absolute values of the y -axis residuals
 382 ranged from 0.6 ppt to 59.0 ppb for CAMS (mean \pm standard deviation = 1.0 ± 3.0 ppb) and 0.1
 383 ppt to 68.1 ppb for ISAF (0.9 ± 3.2 ppb). To differentiate the dependence on HCHO variations
 384 during each TOGA-TOF sampling, a relative standard deviation of 0.7 was used as a cut-off



threshold. For data points with relative standard deviations > 0.7 , residuals ranged from 2.6 ppt to 59.0 ppb (2.7 ± 6.8 ppb) for CAMS and 52.1 ppt to 46.8 ppb (3.7 ± 7.8 ppb) for ISAF. In comparison, for less heterogeneous air masses (i.e., TOGA-merge 1-Hz HCHO with relative standard deviations < 0.7), residuals ranged from 0.6 ppt to 44.1 ppb (0.7 ± 1.8 ppb) for CAMS and from 0.1 ppt to 68.1 ppb (0.6 ± 2.5 ppb) for ISAF. Therefore, the data points with less variable HCHO (i.e., HCHO relative standard deviation < 0.7) showed on average a factor of 4–6 lower residual values, showing that the increased heterogeneity of HCHO in the sampled air masses lead to poorer correlations between TOGA-TOF and the 1-Hz HCHO instruments.

For more accurate comparisons, the CAMS and ISAF HCHO data averages were weighted by the TOGA-TOF sampling volume, factoring in the 50% volume sampling midpoint. Weighted averages of the CAMS and ISAF measured HCHO improved the correlations with TOGA-TOF to give an r^2 of 0.97 (compared to 0.93 for non-weighted averages) for CAMS and 0.96 (compared to 0.91 for non-weighted averages) for ISAF (**Fig. 4c** and **d**). The residuals of the volume-weighted averages were 30% lower for CAMS (range 0.2 ppt to 32.2 ppb and average 0.7 ± 2.0 ppb) and 33% lower for ISAF (range 0.03 ppt to 32 ppb and average 0.6 ± 2.0 ppb). Biases at low mixing ratios significantly improved when using volume-weighted averages with absolute values of the y -intercepts much closer to 0 than the non-weighted averages, at -14.4 ± 42.9 ppt for CAMS (versus -177.4 ± 56.4 ppt) and 9.7 ± 36.8 ppt for ISAF (versus -210.2 ± 59.3 ppt). Comparisons between TOGA-TOF and the UiO PTR-ToF-MS (**Fig. S5**), showed similar results with better agreement when using volume-weighted averages.

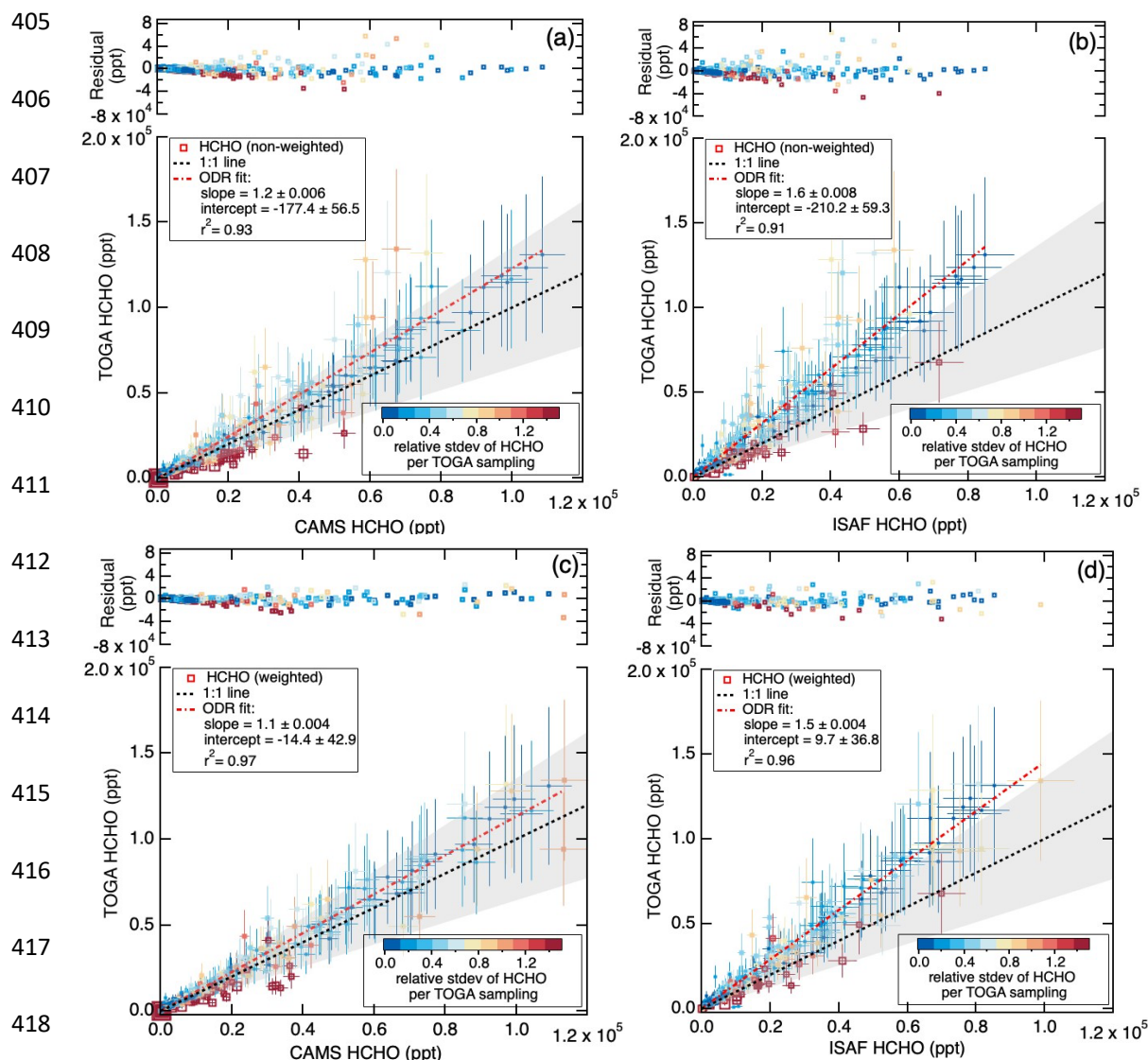


Figure 4. Correlation of measured HCHO (a,c) between TOGA-TOF and CAMS and (b,d) between TOGA-TOF and ISAF. CAMS and ISAF 1-Hz HCHO data were averaged over the TOGA-TOF sampling start and stop times using the (a,b) non-weighted and (c,d) volume-weighted averaging methods. Measurement uncertainties of each measurement technique are shown as error bars. The grey shading around the 1:1 line is the HCHO measurement uncertainties of the two corresponding instruments added in quadrature. Each data point is colored by the relative standard deviation of the 1-Hz HCHO data (standard deviation of 1-Hz averaged HCHO divided by TOGA-TOF HCHO) during the TOGA-TOF sampling period.

The discrepancies of HCHO between different measurement techniques during FIREX-AQ are similar to those shown by Liao et al. (2021), in which a comparison of CAMS vs. ISAF



424 HCHO data had a slope of 1.27. In our study, a comparison of the volume-weighted TOGA-merge
425 CAMS vs. ISAF HCHO from FIREX-AQ has a slope of 1.28, similar to Liao et al. (2021). The
426 minor difference in the slopes is most likely due to the different periods of data selected for analysis
427 as we only included CAMS and ISAF data during TOGA sampling in our analysis. Liao et al.
428 (2021) suggested that the main discrepancies between CAMS and ISAF were driven by the
429 uncertainties in the absolute calibration of the HCHO standards. As mentioned in **Sect. 2.2**, each
430 HCHO measurement technique has been carefully calibrated with HCHO standards. The HCHO
431 calibration standards used by each group were gravimetrically prepared and the absolute
432 concentrations were quantified using optical absorption techniques. As the main purpose of this
433 paper is to validate the TOGA-TOF as a unique technique for measuring HCHO, we will not
434 further explore the reasons for the discrepancies between the instruments.

435 **3.2 Comparison of HCHO NEMR between different instrumental techniques**

436 Normalized excess mixing ratios (NEMR) are used to derive the enhancement of a trace
437 gas within a smoke plume (Yokelson et al., 2013a). **Figure 5** shows HCHO NEMRs derived from
438 Western U.S. fires using the TOGA-TOF, CAMS, and ISAF instrumental techniques with respect
439 to smoke plume physical age ([https://www-air.larc.nasa.gov/cgi-](https://www-air.larc.nasa.gov/cgi-bin/ArcView/firexaq#SCHWARZ.JOSHUA/)
440 [bin/ArcView/firexaq#SCHWARZ.JOSHUA/](https://www-air.larc.nasa.gov/cgi-bin/ArcView/firexaq#SCHWARZ.JOSHUA/)). Based on the instrument uncertainties of both CO
441 and the individual HCHO measurements, the uncertainties of the NEMRs are 35%, 6%, and 10%
442 for TOGA-TOF, CAMS, and ISAF, respectively. The HCHO NEMRs observed during FIREX-
443 AQ from TOGA-TOF were in the range of 12 to 30 ppt ppb⁻¹ CO. These NEMRs were within the
444 wide range observed from previous wildfire biomass burning studies from 2.2 to 46 ppt ppb⁻¹ CO
445 (e.g., Hornbrook et al., 2011 and references therein) and during prescribed burning events in the
446 Southeastern U.S. during FIREX-AQ that ranged from 16 to 29 ppt ppb⁻¹ CO (Travis et al., 2023).



447 The quadratic polynomial fitting of HCHO NEMRs from all three instruments showed that the
 448 NEMRs increased up to ~ 5 h of plume physical age then declined. The age at which the HCHO
 449 NEMRs from each instrument begin to decrease (i.e., the change in the NEMRs with respect to
 450 plume age = 0) are all within 20 minutes of 5 h. This trend with respect to plume physical age
 451 agrees with what Liao et al. (2021) reported for HCHO NEMRs measured by ISAF from individual
 452 fire sources and is driven by the balance of production of HCHO, mainly from VOC oxidation by
 453 OH, and loss of HCHO, mainly from photolysis, throughout the aging of plume (Liao et al., 2021).

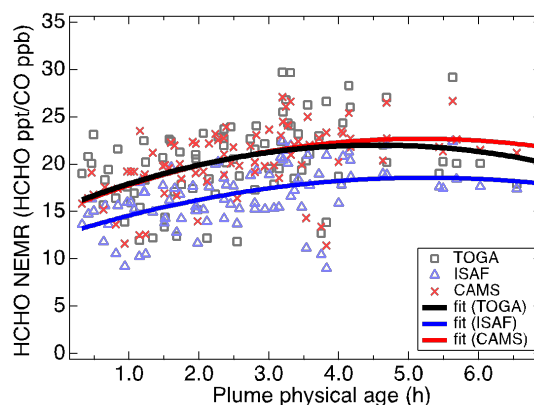


Figure 5. HCHO NEMRs of Western U.S. fires with respect to plume physical age during FIREX-AQ. Quadratic polynomial fittings of NEMRs derived using TOGA-TOF, CAMS, and ISAF HCHO data are shown.

454

455 While the trend with respect to plume physical age was similar using HCHO from the
 456 different instruments, systematic differences were observed. To further investigate the possibility
 457 of systematic differences of the NEMRs derived from the three HCHO instruments, paired *t*-tests
 458 were used as a statistical method to compare two different analytical methods (Yen et al., 2020).
 459 Here we carried out a paired *t*-test on the HCHO NEMRs calculated from the HCHO
 460 measurements from the TOGA-TOF against CAMS and ISAF data. The sample number of the
 461 analysis was equivalent to the number of selected transects for NEMR analysis (86 pairs). The null



hypothesis was whether the HCHO NEMRs from a pair of instruments are the same ($H_0: \hat{f}_1 = \hat{f}_2$), where the absolute value of the t -value (t) higher than the critical t (T_c) rejects the hypothesis. Between the TOGA-TOF and CAMS NEMRs, the analysis yielded $t = -0.42$, $T_c = 1.99$, and p -value = 0.68, retaining the hypothesis (at the $p = 0.05$ (5%) level). Between the TOGA-TOF and ISAF NEMRs, the analysis yielded $t = 11.53$, $T_c = 1.99$, and p -value = 4.68×10^{-19} , rejecting the hypothesis. Between the CAMS and ISAF NEMRs, the analysis yielded $t = 29.84$, $T_c = 1.99$, and p -value = 8.21×10^{-47} , again rejecting the hypothesis. Therefore, both TOGA-TOF and CAMS derived NEMRs had a systematic difference from the ISAF derived NEMRs with a significance at the $p = 0.05$ (5%) level.

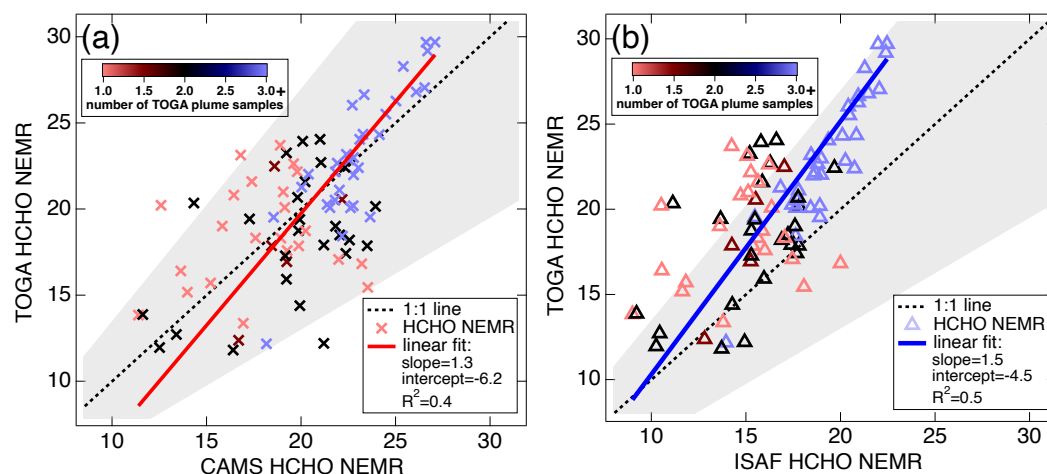


Figure 6. Correlation plots between (a) TOGA-TOF and CAMS and (b) TOGA-TOF and ISAF derived HCHO NEMRs. Orthogonal distance regression fittings of the correlations are shown. The grey shading around the dashed 1:1 line shows the measurement uncertainty (35%) of TOGA-TOF HCHO.

As mentioned in **Sect. 3.1**, systematic biases exist between the HCHO measurement techniques which are likely due to calibration standard differences. As illustrated in **Fig. 5**, these biases are similarly present in the derived HCHO NEMRs. Nonetheless, comparisons between the



475 HCHO NEMRs derived from TOGA-TOF and CAMS (**Fig. 6a**) and TOGA-TOF and ISAF (**Fig.**
476 **6b**) indicate that the correlations are within the uncertainty bounds of the NEMR.

477 3.3 Discussion on TOGA-TOF HCHO NEMRs and their applicability

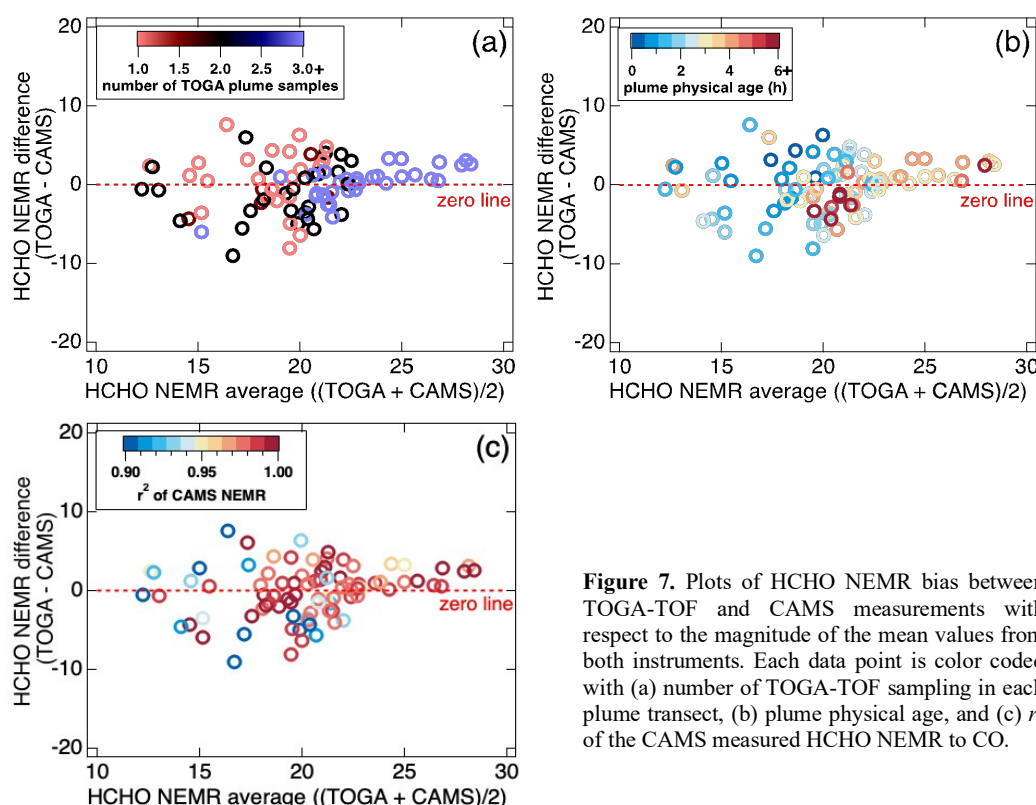


Figure 7. Plots of HCHO NEMR bias between TOGA-TOF and CAMS measurements with respect to the magnitude of the mean values from both instruments. Each data point is color coded with (a) number of TOGA-TOF sampling in each plume transect, (b) plume physical age, and (c) r^2 of the CAMS measured HCHO NEMR to CO.

478

479 The applicability of TOGA-TOF-derived HCHO NEMRs is further explored for different
480 smoke plume conditions. **Figure 7** shows the difference of HCHO NEMRs between TOGA-TOF
481 and CAMS with respect to the averages from the two methods. Similar to **Fig. 5**, **Fig. 7b** shows
482 that the averaged HCHO NEMRs increase with plume physical age. With greater plume physical
483 age, the bias between TOGA-TOF driven HCHO NEMRs to CAMS becomes lower (**Fig. 7b**) and
484 this lower bias corresponds to more TOGA-TOF samples at each plume transect (**Fig. 7a**). With



485 increasing physical age, the smoke plumes studied were generally more dispersed and spatially
486 wider, therefore allowing more TOGA-TOF samples per transect.

487 The reduced bias between the two instrumental techniques with plume physical age can be
488 explained from the evolution of plume heterogeneity with aging, as indicated by the improved r^2
489 of each plume sampling with plume physical age (**Fig. 7c**). Modeling studies of fire plumes
490 (Trentmann et al., 2003a, 2003b; Wang et al., 2021) have shown significant spatial heterogeneity,
491 both vertically and horizontally, of fire plumes with different levels of oxidants (i.e., OH, O₃, NO₃).
492 This plume heterogeneity has also been observed in power plant plumes (Brock et al., 2002). As
493 discussed in Wang et al. (2021), at the early stage of a fire plume, OH levels are severely dampened
494 at the core of the plume, mainly due to attenuation of solar radiation from aerosols, but enhanced
495 at the edges. With aging of the plume, OH levels become more homogeneous (Wang et al., 2021).
496 Liao et al. (2021) showed that HCHO levels observed in fire plumes as they age during FIREX-AQ
497 were primary emissions coupled with subsequent photolytic loss and secondary production,
498 primarily from the oxidation of VOCs with OH. Therefore, with plume physical age, as oxidant
499 levels and photochemistry become more homogeneous, we can expect HCHO NEMRs to be more
500 constant throughout a transect perpendicular to the direction of the smoke transport. As such, the
501 r^2 value of the slope of CAMS HCHO and CO, from which the NEMRs were calculated, is closer
502 to 1 for larger NEMRs (and larger plume physical ages) (**Fig. 7c**). These results demonstrate that
503 the TOGA-TOF data are sufficient for assessing HCHO NEMRs in plumes with physical ages >
504 2–3 h and may result in a small bias in calculated NEMRs for younger, narrower plumes in
505 comparison to those derived using fast HCHO measurement techniques.

506 **4. Conclusions**



507 In this study, we demonstrated the TOGA-TOF as a fast response (< 2 min) GC/MS
508 instrument that can measure HCHO along with > 100 additional C_1 to C_{10} VOCs. During FIREX-
509 AQ, the TOGA-TOF measured a wide range of HCHO mixing ratios with an LLOD of 20 ppt
510 aboard the NASA DC-8. To our knowledge, this technique has not been previously reported for
511 any ambient measurements. The discrete TOGA-TOF HCHO measurements during FIREX-AQ
512 are comparable to the averaged non-discrete 1-Hz HCHO data measured by the CAMS and UiO
513 PTR-ToF-MS instruments while the discrepancies are beyond the combined instrumental
514 uncertainties for the TOGA-TOF and ISAF instruments. The discrepancies between HCHO
515 instrumental techniques during FIREX-AQ are currently believed to be due to differences in
516 calibration standards as quantified by different optical techniques. Using volume-weighted TOGA
517 merge averages of HCHO measured by CAMS, ISAF, and UiO PTR-ToF-MS improved the
518 comparison agreement with TOGA-TOF HCHO observations. Therefore, we strongly encourage
519 the community to use the reported Time_Start, Time_Mid, and Time_Stop values in the TOGA-
520 TOF archived data files to determine volume-weighted averages of concurrent measurements.

521 TOGA-TOF derived NEMRs showed similar trends with plume physical age to what has
522 been reported from ISAF (Liao et al., 2021), with NEMRs increasing with plume ages up to ~ 5 h.
523 Due to its nature of taking discrete subsamples of air masses, small biases may remain in
524 comparison to fast HCHO measurement techniques, especially near strong sources with highly
525 heterogeneous emissions and rapidly varying HCHO production and loss. Nevertheless, the
526 technique used in the TOGA-TOF offers a powerful HCHO-measuring method to the scientific
527 community, with the capability to simultaneously measure > 100 other C_1 - C_{10} VOC species. The
528 wide range of gas-phase VOCs measured with the TOGA-TOF can be used to provide significant
529 insights into understanding the photochemical state of air masses in rural to polluted environments,



530 in addition to verifying satellite observations, three-dimensional modeling, and to compare with
 531 other instrumental techniques.

532 **Data availability.** All data used in this paper are available at [https://www-](https://www-air.larc.nasa.gov/missions/firex-aq/index.html)
 533 [air.larc.nasa.gov/missions/firex-aq/index.html](https://www-air.larc.nasa.gov/missions/firex-aq/index.html)
 534

535 **Author contributions.** ECA conceptualized the project. DJ performed the data analyses and wrote
 536 the manuscript with input from ECA and RSH, RSH, AJH, GD, HSH, JPD, AF, DK, JW, PW,
 537 TFH, GMW, JSC, JP, AW, TM, JBN, FP, JD, CW, JS, ECA performed the measurements, CDH
 538 analyzed the fire smoke ages, AS and EG contributed to the smoke and fuel identification data
 539 product, JHC was the project PI and provided guidance on the analyses.
 540

541 **Competing Interests.** The authors declare they have no conflict of interest. Some authors are
 542 members of the editorial board of AMT.
 543

544 **Acknowledgements.** The authors thank the entire FIREX-AQ Science Team and the NASA DC-8
 545 crew. The authors would also like to thank Hyeong-Ahn Kwon at the University of Suwon for
 546 discussions on HCHO satellite observations.
 547

548 **Financial Support.** Primary support for DJ for this project was provided by the NSF National
 549 Center for Atmospheric Research (NCAR) Advanced Study Program Postdoctoral Fellowship.
 550 This material is based upon work supported by the NSF National Center for Atmospheric
 551 Research, which is a major facility sponsored by the U.S. National Science Foundation under
 552 Cooperative Agreement No. 1852977. This research was also funded in part by NASA award No.
 553 80NSSC18K0633. Additional support was provided by NOAA's Cooperative Agreements with
 554 CIRES NA17OAR4320101 and NA22OAR4320151.
 555

556 References

- 557 Akagi, S. K., Yokelson, R. J., Wiedinmyer, C., Alvarado, M. J., Reid, J. S., Karl, T., Crounse, J.
 558 D., and Wennberg, P. O.: Emission factors for open and domestic biomass burning for use in
 559 atmospheric models, *Atmos. Chem. Phys.*, 11, 4039–4072, [https://doi.org/10.5194/acp-11-4039-](https://doi.org/10.5194/acp-11-4039-2011)
 560 2011, 2011.
- 561 Anderson, D. C., Nicely, J. M., Wolfe, G. M., Hanisco, T. F., Salawitch, R. J., Canty, T. P.,
 562 Dickerson, R. R., Apel, E. C., Baidar, S., Bannan, T. J., Blake, N. J., Chen, D., Dix, B.,
 563 Fernandez, R. P., Hall, S. R., Hornbrook, R. S., Gregory Huey, L., Josse, B., Jöckel, P.,
 564 Kinnison, D. E., Koenig, T. K., Le Breton, M., Marécal, V., Morgenstern, O., Oman, L. D., Pan,
 565 L. L., Percival, C., Plummer, D., Revell, L. E., Rozanov, E., Saiz-Lopez, A., Stenke, A., Sudo,
 566 K., Tilmes, S., Ullmann, K., Volkamer, R., Weinheimer, A. J., and Zeng, G.: Formaldehyde in
 567 the Tropical Western Pacific: Chemical Sources and Sinks, Convective Transport, and
 568 Representation in CAM-Chem and the CCMi Models, *J. Geophys. Res.-Atmos.*, 122, 11201–
 569 11226, <https://doi.org/10.1002/2016JD026121>, 2017.
- 570 Apel, E. C., Hornbrook, R. S., Hills, A. J., Blake, N. J., Barth, M. C., Weinheimer, A., Cantrell,
 571 C., Rutledge, S. A., Basarab, B., Crawford, J., Diskin, G., Homeyer, C. R., Campos, T., Flocke,
 572 F., Fried, A., Blake, D. R., Brune, W., Pollack, I., Peischl, J., Ryerson, T., Wennberg, P. O.,



- 573 Crounse, J. D., Wisthaler, A., Mikoviny, T., Huey, G., Heikes, B., O'Sullivan, D., and Riemer,
574 D. D.: Upper tropospheric ozone production from lightning NO_x-impacted convection: Smoke
575 ingestion case study from the DC3 campaign, *J. Geophys. Res.-Atmos.*, 120, 2505–2523,
576 <https://doi.org/10.1002/2014JD022121>, 2015.
- 577 Bourgeois, I., Peischl, J., Neuman, J. A., Brown, S. S., Allen, H. M., Campuzano-Jost, P.,
578 Coggon, M. M., DiGangi, J. P., Diskin, G. S., Gilman, J. B., Gkatzelis, G. I., Guo, H., Halliday,
579 H. A., Hanisco, T. F., Holmes, C. D., Huey, L. G., Jimenez, J. L., Lamplugh, A. D., Lee, Y. R.,
580 Lindaas, J., Moore, R. H., Nault, B. A., Nowak, J. B., Pagonis, D., Rickly, P. S., Robinson, M.
581 A., Rollins, A. W., Selimovic, V., St. Clair, J. M., Tanner, D., Vasquez, K. T., Veres, P. R.,
582 Warneke, C., Wennberg, P. O., Washenfelder, R. A., Wiggins, E. B., Womack, C. C., Xu, L.,
583 Zarzana, K. J., and Ryerson, T. B.: Comparison of Airborne Measurements of NO, NO₂, HONO,
584 NO_y, and CO during FIREX-AQ, *Atmos. Meas. Tech.*, 15, 4901–4930,
585 <https://doi.org/10.5194/amt-15-4901-2022>, 2022.
- 586 Brock, C. A., Washenfelder, R. A., Trainer, M., Ryerson, T. B., Wilson, J. C., Reeves, J. M.,
587 Huey, L. G., Holloway, J. S., Parrish, D. D., Hübner, G., and Fehsenfeld, F. C.: Particle growth in
588 the plumes of coal-fired power plants, *J. Geophys. Res.-Atmos.*, 107,
589 <https://doi.org/10.1029/2001jd001062>, 2002.
- 590 Cao, H., Fu, T. M., Zhang, L., Henze, D. K., Miller, C. C., Lerot, C., Abad, G. G., De Smedt, I.,
591 Zhang, Q., Van Roozendaal, M., Hendrick, F., Chance, K., Li, J., Zheng, J., and Zhao, Y.:
592 Adjoint inversion of Chinese non-methane volatile organic compound emissions using space-
593 based observations of formaldehyde and glyoxal, *Atmos. Chem. Phys.*, 18, 15017–15046,
594 <https://doi.org/10.5194/acp-18-15017-2018>, 2018.
- 595 Cazorla, M., Wolfe, G. M., Bailey, S. A., Swanson, A. K., Arkinson, H. L., and Hanisco, T. F.: A
596 new airborne laser-induced fluorescence instrument for in situ detection of formaldehyde
597 throughout the troposphere and lower stratosphere, *Atmos. Meas. Tech.*, 8, 541–552,
598 <https://doi.org/10.5194/amt-8-541-2015>, 2015.
- 599 Chan Miller, C., Jacob, D. J., Marais, E. A., Yu, K., Travis, K. R., Kim, P. S., Fisher, J. A., Zhu,
600 L., Wolfe, G. M., Hanisco, T. F., Keutsch, F. N., Kaiser, J., Min, K. E., Brown, S. S.,
601 Washenfelder, R. A., González Abad, G., and Chance, K.: Glyoxal yield from isoprene oxidation
602 and relation to formaldehyde: Chemical mechanism, constraints from SENEX aircraft
603 observations, and interpretation of OMI satellite data, *Atmos. Chem. Phys.*, 17, 8725–8738,
604 <https://doi.org/10.5194/acp-17-8725-2017>, 2017.
- 605 Clafin, M. S., Pagonis, D., Finewax, Z., Handschy, A. V., Day, D. A., Brown, W. L., Jayne, J.
606 T., Worsnop, D. R., Jimenez, J. L., Ziemann, P. J., de Gouw, J., and Lerner, B. M.: An in situ gas
607 chromatograph with automatic detector switching between PTR-and EI-TOF-MS: Isomer-
608 resolved measurements of indoor air, *Atmos. Meas. Tech.*, 14, 133–152,
609 <https://doi.org/10.5194/amt-14-133-2021>, 2021.
- 610 Curci, G., Palmer, P. I., Kurosu, T. P., Chance, K., and Visconti, G.: Estimating European
611 volatile organic compound emissions using satellite observations of formaldehyde from the
612 Ozone Monitoring Instrument, *Atmos. Chem. Phys.*, 10, 11501–11517,
613 <https://doi.org/10.5194/acp-10-11501-2010>, 2010.



- 614 Decker, Z. C. J., Robinson, M. A., Barsanti, K. C., Bourgeois, I., Coggon, M. M., Digangi, J. P.,
615 Diskin, G. S., Flocke, F. M., Franchin, A., Fredrickson, C. D., Gkatzelis, G. I., Hall, S. R.,
616 Halliday, H., Holmes, C. D., Huey, L. G., Lee, Y. R., Lindaas, J., Middlebrook, A. M., Montzka,
617 D. D., Moore, R., Neuman, J. A., Nowak, J. B., Palm, B. B., Peischl, J., Piel, F., Rickly, P. S.,
618 Rollins, A. W., Ryerson, T. B., Schwantes, R. H., Sekimoto, K., Thornhill, L., Thornton, J. A.,
619 Tyndall, G. S., Ullmann, K., Van Rooy, P., Veres, P. R., Warneke, C., Washenfelder, R. A.,
620 Weinheimer, A. J., Wiggins, E., Winstead, E., Wisthaler, A., Womack, C., and Brown, S. S.:
621 Nighttime and daytime dark oxidation chemistry in wildfire plumes: An observation and model
622 analysis of FIREX-AQ aircraft data, *Atmos. Chem. Phys.*, 21, 16293–16317,
623 <https://doi.org/10.5194/acp-21-16293-2021>, 2021.
- 624 Duncan, B. N., Yoshida, Y., Olson, J. R., Sillman, S., Martin, R. V., Lamsal, L., Hu, Y.,
625 Pickering, K. E., Retscher, C., Allen, D. J., and Crawford, J. H.: Application of OMI
626 observations to a space-based indicator of NO_x and VOC controls on surface ozone formation,
627 *Atmos. Environ.*, 44, 2213–2223, <https://doi.org/10.1016/j.atmosenv.2010.03.010>, 2010.
- 628 Fried, A., Walega, J., Weibring, P., Richter, D., Simpson, I. J., Blake, D. R., Blake, N. J.,
629 Meinardi, S., Barletta, B., Hughes, S. C., Crawford, J. H., Diskin, G., Barrick, J., Hair, J., Fenn,
630 M., Wisthaler, A., Mikoviny, T., Woo, J.-H., Park, M., Kim, J., Min, K.-E., Jeong, S., Wennberg,
631 P. O., Kim, M. J., Crounse, J. D., Teng, A. P., Bennett, R., Yang-Martin, M., Shook, M. A.,
632 Huey, G., Tanner, D., Knote, C., Kim, J., Park, R., and Brune, W.: Airborne formaldehyde and
633 volatile organic compound measurements over the Daesan petrochemical complex on Korea's
634 northwest coast during the Korea-United States Air Quality study, *Elem. Sci. Anth.*, 8, 121,
635 <https://doi.org/10.1525/elementa.2020.121>, 2020.
- 636 Gilman, J. B., Lerner, B. M., Kuster, W. C., Goldan, P. D., Warneke, C., Veres, P. R., Roberts, J.
637 M., de Gouw, J. A., Burling, I. R., and Yokelson, R. J.: Biomass burning emissions and potential
638 air quality impacts of volatile organic compounds and other trace gases from fuels common in
639 the US, *Atmos. Chem. Phys.*, 15, 13915–13938, <https://doi.org/10.5194/acp-15-13915-2015>,
640 2015.
- 641 Gilpin, T., Apel, E., Fried, A., Wert, B., Calvert, J., Genfa, Z., Dasgupta, P., Harder, J. W.,
642 Heikes, B., Hopkins, B., Westberg, H., Kleindienst, T., Lee, Y. N., Zhou, X., Lonneman, W., and
643 Sewell, S.: Intercomparison of six ambient [CH₂O] measurement techniques, *J. Geophys. Res.-*
644 *Atmos.*, 102, 21161–21188, <https://doi.org/10.1029/97jd01314>, 1997.
- 645 Gkatzelis, G. I., Coggon, M. M., Stockwell, C. E., Hornbrook, R. S., Allen, H., Apel, E. C., Bela,
646 M. M., Blake, D. R., Bourgeois, I., Brown, S. S., Campuzano-Jost, P., Clair, J. M. S., Crawford,
647 J. H., Crounse, J. D., Day, D. A., Digangi, J. P., Diskin, G. S., Fried, A., Gilman, J. B., Guo, H.,
648 Hair, J. W., Halliday, H. S., Hanisco, T. F., Hannun, R., Hills, A., Huey, L. G., Jimenez, J. L.,
649 Katich, J. M., Lamplugh, A., Lee, Y. R., Liao, J., Lindaas, J., Mckeen, S. A., Mikoviny, T.,
650 Nault, B. A., Neuman, J. A., Nowak, J. B., Pagonis, D., Peischl, J., Perring, A. E., Piel, F.,
651 Rickly, P. S., Robinson, M. A., Rollins, A. W., Ryerson, T. B., Schueneman, M. K., Schwantes,
652 R. H., Schwarz, J. P., Sekimoto, K., Selimovic, V., Shingler, T., Tanner, D. J., Tomsche, L.,
653 Vasquez, K. T., Veres, P. R., Washenfelder, R., Weibring, P., Wennberg, P. O., Wisthaler, A.,
654 Wolfe, G. M., Womack, C. C., Xu, L., Ball, K., Yokelson, R. J., and Warneke, C.:
655 Parameterizations of US Wildfire and Prescribed Fire Emission Ratios and Emission Factors
656 Based on FIREX-AQ Aircraft Measurements, *Atmos. Chem. Phys.*, 24, 929–956,
657 <https://doi.org/10.5194/acp-24-929-2024>, 2024.



- 658 Green, J. R., Fiddler, M. N., Fibiger, D. L., McDuffie, E. E., Aquino, J., Campos, T., Shah, V.,
659 Jaeglé, L., Thornton, J. A., DiGangi, J. P., Wolfe, G. M., Bililign, S., and Brown, S. S.:
660 Wintertime Formaldehyde: Airborne Observations and Source Apportionment Over the Eastern
661 United States, *J. Geophys. Res.-Atmos.*, 126, e2020JD033518,
662 <https://doi.org/10.1029/2020JD033518>, 2021.
- 663 Hopkins, J. R., Still, T., Al-Haider, S., Fisher, I. R., Lewis, A. C., and Seakins, P. W.: A
664 simplified apparatus for ambient formaldehyde detection via GC-pHID, *Atmos. Environ.*, 37,
665 2557–2565, [https://doi.org/10.1016/S1352-2310\(03\)00178-X](https://doi.org/10.1016/S1352-2310(03)00178-X), 2003.
- 666 Hornbrook, R. S., Blake, D. R., Diskin, G. S., Fried, A., Fuelberg, H. E., Meinardi, S., Mikoviny,
667 T., Richter, D., Sachse, G. W., Vay, S. A., Walega, J., Weibring, P., Weinheimer, A. J.,
668 Wiedinmyer, C., Wisthaler, A., Hills, A., Riemer, D. D., and Apel, E. C.: Observations of
669 nonmethane organic compounds during ARCTAS-Part 1: Biomass burning emissions and plume
670 enhancements, *Atmos. Chem. Phys.*, 11, 11103–11130, [https://doi.org/10.5194/acp-11-11103-](https://doi.org/10.5194/acp-11-11103-2011)
671 2011, 2011.
- 672 Hunter, M. C., Bartle, K. D., Seakins, P. W., and Lewis, A. C.: Direct measurement of
673 atmospheric formaldehyde using gas chromatography-pulsed discharge ionisation detection,
674 *Anal. Commun.*, 36, 101–104, <https://doi.org/10.1039/A809762C>, 1999.
- 675 Isaacman-VanWertz, G., Sueper, D. T., Aikin, K. C., Lerner, B. M., Gilman, J. B., de Gouw, J.
676 A., Worsnop, D. R., and Goldstein, A. H.: Automated single-ion peak fitting as an efficient
677 approach for analyzing complex chromatographic data, *J. Chromatogr. A*, 1529, 81–92,
678 <https://doi.org/10.1016/j.chroma.2017.11.005>, 2017.
- 679 Jaeglé, L., Shah, V., Thornton, J. A., Lopez-Hilfiker, F. D., Lee, B. H., McDuffie, E. E., Fibiger,
680 D., Brown, S. S., Veres, P., Sparks, T. L., Ebben, C. J., Wooldridge, P. J., Kenagy, H. S., Cohen,
681 R. C., Weinheimer, A. J., Campos, T. L., Montzka, D. D., Digangi, J. P., Wolfe, G. M., Hanisco,
682 T., Schroder, J. C., Campuzano-Jost, P., Day, D. A., Jimenez, J. L., Sullivan, A. P., Guo, H., and
683 Weber, R. J.: Nitrogen Oxides Emissions, Chemistry, Deposition, and Export Over the Northeast
684 United States During the WINTER Aircraft Campaign, *J. Geophys. Res.-Atmos.*, 123, 12368–
685 12393, <https://doi.org/10.1029/2018JD029133>, 2018.
- 686 Kaiser, J., Jacob, D. J., Zhu, L., Travis, K. R., Fisher, J. A., González Abad, G., Zhang, L.,
687 Zhang, X., Fried, A., Crounse, J. D., Clair, J. M. S., and Wisthaler, A.: High-resolution inversion
688 of OMI formaldehyde columns to quantify isoprene emission on ecosystem-relevant scales:
689 Application to the southeast US, *Atmos. Chem. Phys.*, 18, 5483–5497,
690 <https://doi.org/10.5194/acp-18-5483-2018>, 2018.
- 691 Koss, A. R., Sekimoto, K., Gilman, J. B., Selimovic, V., Coggon, M. M., Zarzana, K. J., Yuan,
692 B., Lerner, B. M., Brown, S. S., Jimenez, J. L., Krechmer, J., Roberts, J. M., Warneke, C.,
693 Yokelson, R. J., and de Gouw, J.: Non-methane organic gas emissions from biomass burning:
694 Identification, quantification, and emission factors from PTR-ToF during the FIREX 2016
695 laboratory experiment, *Atmos. Chem. Phys.*, 18, 3299–3319, [https://doi.org/10.5194/acp-18-](https://doi.org/10.5194/acp-18-3299-2018)
696 3299–2018, 2018.
- 697 Kwon, H. A., Park, R. J., Oak, Y. J., Nowlan, C. R., Janz, S. J., Kowalewski, M. G., Fried, A.,
698 Walega, J., Bates, K. H., Choi, J., Blake, D. R., Wisthaler, A., and Woo, J. H.: Top-down
699 estimates of anthropogenic VOC emissions in South Korea using formaldehyde vertical column



- 700 densities from aircraft during the KORUS-AQ campaign, *Elem. Sci. Anth.*, 9, 00109,
701 <https://doi.org/10.1525/elementa.2021.00109>, 2021.
- 702 Lee, M., Heikes, B. G., Jacob, D. J., Sachse, G., and Anderson, B.: Hydrogen peroxide, organic
703 hydroperoxide, and formaldehyde as primary pollutants from biomass burning, *J. Geophys. Res.-*
704 *Atmos.*, 102, 1301–1309, <https://doi.org/10.1029/96JD01709>, 1997.
- 705 Lerner, B. M., Gilman, J. B., Aikin, K. C., Atlas, E. L., Goldan, P. D., Graus, M., Hendershot,
706 R., Isaacman-VanWertz, G. A., Koss, A., Kuster, W. C., Lueb, R. A., Mclaughlin, R. J., Peischl,
707 J., Sueper, D., Ryerson, T. B., Tokarek, T. W., Warneke, C., Yuan, B., and de Gouw, J. A.: An
708 improved, automated whole air sampler and gas chromatography mass spectrometry analysis
709 system for volatile organic compounds in the atmosphere, *Atmos. Meas. Tech.*, 10, 291–313,
710 <https://doi.org/10.5194/amt-10-291-2017>, 2017.
- 711 Liao, J., Wolfe, G. M., Hannun, R. A., St. Clair, J. M., Hanisco, T. F., Gilman, J. B., Lamplugh,
712 A., Selimovic, V., Diskin, G. S., Nowak, J. B., Halliday, H. S., Digangi, J. P., Hall, S. R.,
713 Ullmann, K., Holmes, C. D., Fite, C. H., Agastra, A., Ryerson, T. B., Peischl, J., Bourgeois, I.,
714 Warneke, C., Coggon, M. M., Gkatzelis, G. I., Sekimoto, K., Fried, A., Richter, D., Weibring, P.,
715 Apel, E. C., Hornbrook, R. S., Brown, S. S., Womack, C. C., Robinson, M. A., Washenfelder, R.
716 A., Veres, P. R., and Neuman, J. A.: Formaldehyde evolution in US wildfire plumes during the
717 Fire Influence on Regional to Global Environments and Air Quality experiment (FIREX-AQ),
718 *Atmos. Chem. Phys.*, 21, 18319–18331, <https://doi.org/10.5194/acp-21-18319-2021>, 2021.
- 719 Liao, J., Wolfe, G. M., Kotsakis, A. E., Nicely, J. M., St. Clair, J. M., Hanisco, T. F., Abad, G.
720 G., Nowlan, C. R., Ayazpour, Z., De Smedt, I., Apel, E. C., Hornbrook, R. S.: Validation of
721 formaldehyde products from three satellite retrievals (OMI SAO, OMPS-NPP SAO, and OMI
722 BIRA) in the marine atmosphere with four seasons of Atmospheric Tomography Mission
723 (ATom) aircraft observations, *Atmos. Meas. Tech.*, 18, 1–16, [https://doi.org/10.5194/amt-18-1-](https://doi.org/10.5194/amt-18-1-2025)
724 [2025](https://doi.org/10.5194/amt-18-1-2025), 2025.
- 725 Luecken, D. J., Hutzell, W. T., Strum, M. L., and Pouliot, G. A.: Regional sources of
726 atmospheric formaldehyde and acetaldehyde, and implications for atmospheric modeling, *Atmos.*
727 *Environ.*, 47, 477–490, <https://doi.org/10.1016/j.atmosenv.2011.10.005>, 2012.
- 728 Luecken, D. J., Napelenok, S. L., Strum, M., Scheffe, R., and Phillips, S.: Sensitivity of Ambient
729 Atmospheric Formaldehyde and Ozone to Precursor Species and Source Types Across the
730 United States, *Environ. Sci. Technol.*, 52, 4668–4675, <https://doi.org/10.1021/acs.est.7b05509>,
731 2018.
- 732 Martin, R. V., Fiore, A. M., and Van Donkelaar, A.: Space-based diagnosis of surface ozone
733 sensitivity to anthropogenic emissions, *Geophys. Res. Lett.*, 31, L06120,
734 <https://doi.org/10.1029/2004GL019416>, 2004.
- 735 Müller, M., Mikoviny, T., Feil, S., Haidacher, S., Hanel, G., Hartungen, E., Jordan, A., Märk, L.,
736 Mutschlechner, P., Schottkowsky, R., Sulzer, P., Crawford, J. H., and Wisthaler, A.: A compact
737 PTR-ToF-MS instrument for airborne measurements of volatile organic compounds at high
738 spatiotemporal resolution, *Atmos. Meas. Tech.*, 7, 3763–3772, [https://doi.org/10.5194/amt-7-](https://doi.org/10.5194/amt-7-3763-2014)
739 [3763-2014](https://doi.org/10.5194/amt-7-3763-2014), 2014.
- 740 Müller, M., Anderson, B. E., Beyersdorf, A. J., Crawford, J. H., Diskin, G. S., Eichler, P., Fried,
741 A., Keutsch, F. N., Mikoviny, T., Thornhill, K. L., Walega, J. G., Weinheimer, A. J., Yang, M.,



- 742 Yokelson, R. J., and Wisthaler, A.: In situ measurements and modeling of reactive trace gases in
743 a small biomass burning plume, *Atmos. Chem. Phys.*, 16, 3813–3824,
744 <https://doi.org/10.5194/acp-16-3813-2016>, 2016.
- 745 National Research Council (US) Committee on Toxicology: Formaldehyde - An Assessment of
746 Its Health Effects, Washington (DC), 1980.
- 747 Nussbaumer, C. M., Crowley, J. N., Schuladen, J., Williams, J., Hafermann, S., Reiffs, A.,
748 Axinte, R., Harder, H., Ernest, C., Novelli, A., Sala, K., Martinez, M., Mallik, C., Tomsche, L.,
749 Plass-Dülmer, C., Bohn, B., Lelieveld, J., and Fischer, H.: Measurement report: Photochemical
750 production and loss rates of formaldehyde and ozone across Europe, *Atmos. Chem. Phys.*, 21,
751 18413–18432, <https://doi.org/10.5194/acp-21-18413-2021>, 2021.
- 752 Palmer, P. I., Jacob, D. J., Fiore, A. M., Martin, R. V., Chance, K., and Kurosu, T. P.: Mapping
753 isoprene emissions over North America using formaldehyde column observations from space, *J.*
754 *Geophys. Res.-Atmos.*, 108, 4180, <https://doi.org/10.1029/2002jd002153>, 2003.
- 755 Pfister, G., Wang, C. T., Barth, M., Flocke, F., Vizuete, W., and Walters, S.: Chemical
756 Characteristics and Ozone Production in the Northern Colorado Front Range, *J. Geophys. Res.-*
757 *Atmos.*, 124, 13397–13419, <https://doi.org/10.1029/2019JD030544>, 2019.
- 758 Possanzini, M., Palo, V. di, and Cecinato, A.: Sources and photodecomposition of formaldehyde
759 and acetaldehyde in Rome ambient air, *Atmos. Environ.*, 36, 3195–3201,
760 [https://doi.org/10.1016/S1352-2310\(02\)00192-9](https://doi.org/10.1016/S1352-2310(02)00192-9), 2002.
- 761 Rice, A. L. and Quay, P. D.: Isotopic analysis of atmospheric formaldehyde by gas
762 chromatography isotope ratio mass spectrometry, *Anal. Chem.*, 78, 6320–6326,
763 <https://doi.org/10.1021/ac0602367>, 2006.
- 764 Richter, D., Weibring, P., Walega, J. G., Fried, A., Spuler, S. M., and Taubman, M. S.: Compact
765 highly sensitive multi-species airborne mid-IR spectrometer, *Appl. Phys. B*, 119, 119–131,
766 <https://doi.org/10.1007/s00340-015-6038-8>, 2015.
- 767 Robinson, M. A., Decker, Z. C. J., Barsanti, K. C., Coggon, M. M., Flocke, F. M., Franchin, A.,
768 Fredrickson, C. D., Gilman, J. B., Gkatzelis, G. I., Holmes, C. D., Lamplugh, A., Lavi, A.,
769 Middlebrook, A. M., Montzka, D. M., Palm, B. B., Peischl, J., Pierce, B., Schwantes, R. H.,
770 Sekimoto, K., Selimovic, V., Tyndall, G. S., Thornton, J. A., Van Rooy, P., Warneke, C.,
771 Weinheimer, A. J., and Brown, S. S.: Variability and Time of Day Dependence of Ozone
772 Photochemistry in Western Wildfire Plumes, *Environ. Sci. Technol.*, 55, 10280–10290,
773 <https://doi.org/10.1021/acs.est.1c01963>, 2021.
- 774 Sachse, G. W., Hill, G. F., Wade, L. O., and Perry, M. G.: Fast-response, high-precision carbon
775 monoxide sensor using a tunable diode laser absorption technique, *J. Geophys. Res.-Atmos.*, 92,
776 2071–2081, <https://doi.org/10.1029/JD092iD02p02071>, 1987.
- 777 Sagebiel, J. C., Zielinska, B., Pierson, W. R., and Gertler, A. W.: Real-world emissions and
778 calculated reactivities of organic species from motor vehicles, *Atmos. Environ.*, 30, 2287–2296,
779 [https://doi.org/10.1016/1352-2310\(95\)00117-4](https://doi.org/10.1016/1352-2310(95)00117-4), 1996.
- 780 Schroeder, J. R., Crawford, J. H., Fried, A., Walega, J., Weinheimer, A., Wisthaler, A., Müller,
781 M., Mikoviny, T., Chen, G., Shook, M., Blake, D. R., and Tonnesen, G. S.: New insights into the



- 782 column $\text{CH}_2\text{O}/\text{NO}_2$ ratio as an indicator of near-surface ozone sensitivity, *J. Geophys. Res.-*
783 *Atmos.*, 122, 8885–8907, <https://doi.org/10.1002/2017JD026781>, 2017.
- 784 Seinfeld, J. H. and Pandis, S. N.: *Atmospheric Chemistry and Physics: From Air Pollution to*
785 *Climate Change*, 2nd ed., Wiley-Interscience, Hoboken, NJ, 2006.
- 786 Selimovic, V., Yokelson, R. J., McMeeking, G. R., and Coefield, S.: In situ measurements of
787 trace gases, PM, and aerosol optical properties during the 2017 NW US wildfire smoke event,
788 *Atmos. Chem. Phys.*, 19, 3905–3926, <https://doi.org/10.5194/acp-19-3905-2019>, 2019.
- 789 Souri, A. H., Nowlan, C. R., Wolfe, G. M., Lamsal, L. N., Miller, C., González Abad, G., Janz,
790 S. J., Fried, A., Blake, D. R., Weinheimer, A. J., Diskin, G. S., Liu, X., and Chance, K.:
791 Revisiting the effectiveness of HCHO/NO_2 ratios for inferring ozone sensitivity to its precursors
792 using high resolution airborne remote sensing observations in a high ozone episode during the
793 KORUS-AQ campaign, *Atmos. Environ.*, 224, 117341,
794 <https://doi.org/10.1016/j.atmosenv.2020.117341>, 2020.
- 795 Souri, A. H., Johnson, M. S., Wolfe, G. M., Crawford, J. H., Fried, A., Wisthaler, A., Brune, W.
796 H., Blake, D. R., Weinheimer, A. J., Verhoelst, T., Compernelle, S., Pinardi, G., Vigouroux, C.,
797 Langerock, B., Choi, S., Lamsal, L., Zhu, L., Sun, S., Cohen, R. C., Min, K. E., Cho, C., Philip,
798 S., Liu, X., and Chance, K.: Characterization of errors in satellite-based HCHO/NO_2
799 tropospheric column ratios with respect to chemistry, column-to-PBL translation, spatial
800 representation, and retrieval uncertainties, *Atmos. Chem. Phys.*, 23, 1963–1986,
801 <https://doi.org/10.5194/acp-23-1963-2023>, 2023.
- 802 Stavrakou, T., Müller, J.-F., De Smedt, I., Van Roozendael, M., van der Werf, G. R., Giglio, L.,
803 and Guenther, A.: Evaluating the performance of pyrogenic and biogenic emission inventories
804 against one decade of space-based formaldehyde columns, *Atmos. Chem. Phys.*, 1037–1060,
805 <https://doi.org/10.5194/acp-9-1037-2009>, 2009.
- 806 Travis, K. R., Crawford, James. H., Soja, A. J., Gargulinski, E. M., Moore, R. H., Wiggins, E.
807 B., Diskin, G. S., DiGangi, J. P., Nowak, J. B., Halliday, H., Yokelson, R. J., McCarty, J. L.,
808 Simpson, I. J., Blake, D. R., Neinardi, S., Hornbrook, R. S., Apel, E. C., Hills, A. J., Warneke,
809 C., Coggon, M. M., Rollins, A. W., Gilman, J. B., Womack, C. C., Robinson, M. A., Katich, J.
810 M., Peischl, J., Gkatzelis, G. I., Bourgeois, I., Rickly, P. S., Lamplugh, A., Dibb, J. E., Jimenez,
811 J. L., Campuzano-Jost, P., Day, D. A., Guo, H., Pagonis, D., Wennberg, P. O., Crounse, J. D.,
812 Xu, L., Hanisco, T. F., Wolfe, G. M., Liao, J., St. Clair, J. M., Nault, B. A., Fried, A., and
813 Perring, A. E.: Emission Factors for Crop Residue and Prescribed Fires in the Eastern US during
814 FIREX-AQ, *J. Geophys. Res.-Atmos.*, 128, e2023JD039309,
815 <https://doi.org/10.1029/2023JD039309>, 2023.
- 816 Trentmann, J., Andreae, M. O., and Graf, H. F.: Chemical processes in a young biomass-burning
817 plume, *J. Geophys. Res.-Atmos.*, 108, 4705, <https://doi.org/10.1029/2003jd003732>, 2003a.
- 818 Trentmann, J., Früh, B., Boucher, O., Trautmann, T., and Andreae, M. O.: Three-dimensional
819 solar radiation effects on the actinic flux field in a biomass-burning plume, *J. Geophys. Res.-*
820 *Atmos.*, 108, 4558, <https://doi.org/10.1029/2003jd003422>, 2003b.
- 821 Viskari, E.-L., Vartiainen, M., and Pasanen, P.: Seasonal and diurnal variation in formaldehyde
822 and acetaldehyde concentrations along a highway in Eastern Finland, *Atmos. Environ.*, 34, 917–
823 923, [https://doi.org/10.1016/S1352-2310\(99\)00307-6](https://doi.org/10.1016/S1352-2310(99)00307-6), 2000.



- 824 Wang, S., Coggon, M. M., Gkatzelis, G. I., Warneke, C., Bourgeois, I., Ryerson, T., Peischl, J.,
825 Veres, P. R., Neuman, J. A., Hair, J., Shingler, T., Fenn, M., Diskin, G., Huey, L. G., Lee, Y. R.,
826 Apel, E. C., Hornbrook, R. S., Hills, A. J., Hall, S. R., Ullmann, K., Bela, M. M., Trainer, M. K.,
827 Kumar, R., Orlando, J. J., Flocke, F. M., and Emmons, L. K.: Chemical Tomography in a Fresh
828 Wildland Fire Plume: A Large Eddy Simulation (LES) Study, *J. Geophys. Res.-Atmos.*, 126,
829 e2021JD035203, <https://doi.org/10.1029/2021JD035203>, 2021.
- 830 Warneke, C., McKeen, S. A., de Gouw, J. A., Goldan, P. D., Kuster, W. C., Holloway, J. S.,
831 Williams, E. J., Lerner, B. M., Parrish, D. D., Trainer, M., Fehsenfeld, F. C., Kato, S., Atlas, E.
832 L., Baker, A., and Blake, D. R.: Determination of urban volatile organic compound emission
833 ratios and comparison with an emissions database, *J. Geophys. Res.-Atmos.*, 112, D10S47,
834 <https://doi.org/10.1029/2006JD007930>, 2007.
- 835 Warneke, C., Schwarz, J. P., Dibb, J., Kalashnikova, O., Frost, G., Al-Saad, J., Brown, S. S.,
836 Brewer, Wm. A., Soja, A., Seidel, F. C., Washenfelder, R. A., Wiggins, E. B., Moore, R. H.,
837 Anderson, B. E., Jordan, C., Yacovitch, T. I., Herndon, S. C., Liu, S., Kuwayama, T., Jaffe, D.,
838 Johnston, N., Selimovic, V., Yokelson, R., Giles, D. M., Holben, B. N., Goloub, P., Popovici, I.,
839 Trainer, M., Kumar, A., Pierce, R. B., Fahey, D., Roberts, J., Gargulinski, E. M., Peterson, D. A.,
840 Ye, X., Thapa, L. H., Saide, P. E., Fite, C. H., Holmes, C. D., Wang, S., Coggon, M. M., Decker,
841 Z. C. J., Stockwell, C. E., Xu, L., Gkatzelis, G., Aikin, K., Lefer, B., Kaspari, J., Griffin, D.,
842 Zeng, L., Weber, R., Hastings, M., Chai, J., Wolfe, G. M., Hanisco, T. F., Liao, J., Campuzano
843 Jost, P., Guo, H., Jimenez, J. L., Crawford, J., and Team, T. F.-A. S.: Fire Influence on Regional
844 to Global Environments and Air Quality (FIREX-AQ), *J. Geophys. Res.-Atmos.*, 128,
845 e2022JD037758, <https://doi.org/10.1029/2022JD037758>, 2023.
- 846 Wolfe, G. M., Kaiser, J., Hanisco, T. F., Keutsch, F. N., de Gouw, J. A., Gilman, J. B., Graus,
847 M., Hatch, C. D., Holloway, J., Horowitz, L. W., Lee, B. H., Lerner, B. M., Lopez-Hilfiker, F.,
848 Mao, J., Marvin, M. R., Peischl, J., Pollack, I. B., Roberts, J. M., Ryerson, T. B., Thornton, J. A.,
849 Veres, P. R., and Warneke, C.: Formaldehyde production from isoprene oxidation across NO_x
850 regimes, *Atmos. Chem. Phys.*, 16, 2597–2610, <https://doi.org/10.5194/acp-16-2597-2016>, 2016.
- 851 Yen, J., Leber, D., and Pibida, L.: Comparing Instruments, Gaithersburg, MD,
852 <https://doi.org/10.6028/NIST.TN.2106>, 2020.
- 853 Yokelson, R. J., Andreae, M. O., and Akagi, S. K.: Pitfalls with the use of enhancement ratios or
854 normalized excess mixing ratios measured in plumes to characterize pollution sources and aging,
855 *Atmos. Meas. Tech.*, 6, 2155–2158, <https://doi.org/10.5194/amt-6-2155-2013>, 2013a.
- 856 Yokelson, R. J., Burling, I. R., Gilman, J. B., Warneke, C., Stockwell, C. E., de Gouw, J., Akagi,
857 S. K., Urbanski, S. P., Veres, P., Roberts, J. M., Kuster, W. C., Reardon, J., Griffith, D. W. T.,
858 Johnson, T. J., Hosseini, S., Miller, J. W., Cocker, D. R., Jung, H., and Weise, D. R.: Coupling
859 field and laboratory measurements to estimate the emission factors of identified and unidentified
860 trace gases for prescribed fires, *Atmos. Chem. Phys.*, 13, 89–116, <https://doi.org/10.5194/acp-13-89-2013>, 2013b.
- 862 Zhang, H., Li, J., Ying, Q., Guven, B. B., and Olaguer, E. P.: Source apportionment of
863 formaldehyde during TexAQS 2006 using a source-oriented chemical transport model, *J.*
864 *Geophys. Res.-Atmos.*, 118, 1525–1535, <https://doi.org/10.1002/jgrd.50197>, 2013.



865 Zhu, L., Jacob, D. J., Kim, P. S., Fisher, J. A., Yu, K., Travis, K. R., Mickley, L. J., Yantosca, R.
866 M., Sulprizio, M. P., De Smedt, I., Abad, G. G., Chance, K., Li, C., Ferrare, R., Fried, A., Hair, J.
867 W., Hanisco, T. F., Richter, D., Scarino, A. J., Walega, J., Weibring, P., and Wolfe, G. M.:
868 Observing atmospheric formaldehyde (HCHO) from space: Validation and intercomparison of
869 six retrievals from four satellites (OMI, GOME2A, GOME2B, OMPS) with SEAC⁴RS aircraft
870 observations over the southeast US, *Atmos. Chem. Phys.*, 16, 13477–13490,
871 <https://doi.org/10.5194/acp-16-13477-2016>, 2016.

872 Zhu, L., Jacob, D. J., Keutsch, F. N., Mickley, L. J., Scheffe, R., Strum, M., González Abad, G.,
873 Chance, K., Yang, K., Rappenglück, B., Millet, D. B., Baasandorj, M., Jaeglé, L., and Shah, V.:
874 Formaldehyde (HCHO) As a Hazardous Air Pollutant: Mapping Surface Air Concentrations
875 from Satellite and Inferring Cancer Risks in the United States, *Environ. Sci. Technol.*, 51, 5650–
876 5657, <https://doi.org/10.1021/acs.est.7b01356>, 2017.

877